ISSN (Print) 1226-1750
ISSN (Online) 2233-6656
Journal of Magnetics 25(4), 475-484 (2020) https://doi.org/10.4283/JMAG.2020.25.4.475

Performance Evaluation of Permanent Magnet Synchronous Machines according to Rotor Types for Machine Tool Application

Yu-Seop Park*

Department of Electrical Engineering, Korea National University of Transportation, Chungju 27469, Republic of Korea

(Received 18 September 2020, Received in final form 19 December 2020, Accepted 21 December 2020)

This paper deals with comparative investigation on permanent magnet synchronous machines (PMSMs) with identical stator structure based on electromagnetic field analysis. By considering their rotor types with rare-earth magnets, the influence of space vector pulse width modulation inverter on machine performance is investigated based on the predicted phase current. As analysis models, a surface-mounted PMSM (SPMSM) with parallel magnetization, a SPMSM with Halbach magnetization, and an interior PMSM (IPMSM) are employed for their comparison. For their effective investigation, machines are designed to have identical equivalent circuit parameters, such as resistance and induced voltage in no-load condition. Based on the dynamic modeling of the SVPWM inverter, the phase current is predicted, and their output characteristic, power losses and radial force density are comparatively investigated by electromagnetic field analysis. In addition, with a manufactured machine, the validity of this paper is demonstrated as well.

Keywords : IPMSM, performance evaluation, SPMSM

1. Introduction

Various types of motors can be employed as the spindle motor of machine tool systems, and it requires high power density in wide operation speed range. As it is very well known, the induction motor is one of the representative machines for the application. With high conductivity of copper bar and low core loss of silicon plate, the machine shows high performance, recently. This type of machines introduced in [1] for spindle systems, and the authors performed electric and mechanical analysis and tests of the 10 (kW) machine at 30,000 (rpm).

On the contrary, permanent magnet synchronous machines (PMSMs) are also actively applied in various industrial applications requiring high torque density and efficiency, and it is also attractive for spindle systems. As it is very well known, the PMSMs can be divided into a surface-mounted PMSM (SPMSM) and an interior PMSM (IPMSM) according to the position of PMs. Since each one has advantages and disadvantages, the determination of machine types is very important for motor designers. Previous studies also reported that the PMSMs are also employed as the spindle motor in machine tool systems. In [2], the authors investigated the 1.5(kW) machine at 60,000(rpm), and the motor type was SPMSM with sleeve. Since the eddy current is generated in PMs, this study proposed the method with PM segmentation to reduce the rotor loss.

Besides, when it comes to the magnetization patterns of PMs, parallel magnetization is widely applied while the study on Halbach magnetization is also actively performed. Halbach magnetization pattern has several benefits, such as sinusoidal filed distribution [3], higher air-gap flux density [4], shelf-shielding [5], so it is popular for various applications with SPMSMs. In particular, when the rotor core should be very thin or when a non-magnetic material is used, the Halbach magnetization is one of the attractive candidates. In this paper, it is also investigated under various analysis conditions.

On the other hand, their control methods have been reported in plenty of previous studies. Among those various control methods, brushless DC motor drive (BLDCMD) and AC synchronous motor drive (ACSMD) are very widely employed [6]. In particular, for ACSMD, the space vector pulse width modulation (SVPWM) inverter is one of the most popular topology for effective motor control systems. However, its switching process can have high influence on motor performance, such as

©The Korean Magnetics Society. All rights reserved.
*Corresponding author: Tel: +82-43-841-5148
Fax: +82-43-841-5140, e-mail: yspark@ut.ac.kr

© 2020 Journal of Magnetics

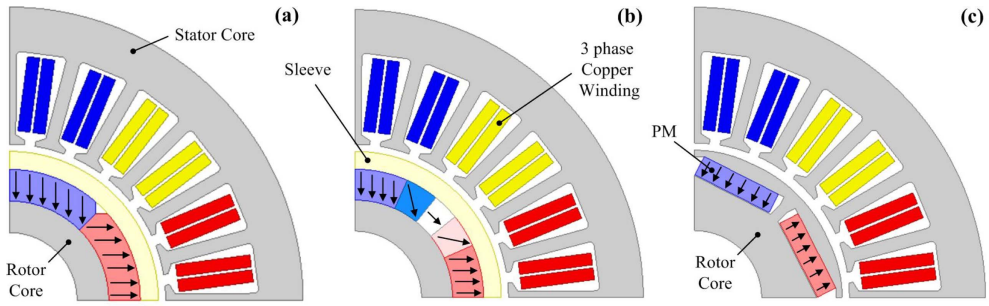

Fig. 1. (Color online) Electromagnetic structure of analysis models: (a) Type A (SPMSM with parallel magnetization), (b) Type B (SPMSM with Halbach Magnetization), (c) Type C (IPMSM with parallel Magnetization).

power losses. In [7], the eddy current loss was analytically investigated.

So far, the comparison of PMSMs according to motor types has been widely studied, but the performance evaluation by considering the influence of the switching frequency on machine types with different magnetization patterns was seldom performed. Therefore, in this paper, two SPMSMs according to magnetization patterns and one IPMSM are comparatively investigated. The main objective of this study is to prove the evaluation results according to mentioned rotor types with different shaft size. Under the identical machine size and parameter conditions, machine performances are compared, and experimental verification will support the analysis results.

2. Analysis Models according to Rotor Topology and Motor Parameter Derivation

2.1. Analysis Models

Figure 1 shows the electromagnetic structure of analysis models according to rotor types while they have identical stator with three-phase coil winding. As shown in the figure, the number of poles is 4, and the number of stator slots is 24. Largely, those machines are divided into two categories. In other words, Type A and Type B are SPMSMs while they have PMs with parallel and Halbach magnetization patterns, respectively. On the other hand, Type C presents the IPMSM with parallel-magnetized PMs in rectangular shape. Here, the machines have identical stator, and the outer diameter of rotor and the axial length are identical for reasonable comparison. In Table 1, more detailed specifications are provided. As mentioned before, this paper also considers their size conditions, and the specifications in Table 1 are for original models. More specific size conditions are addressed later. In the original conditions, the induced voltage and resistance are designed to be identical.

In this study, the machines employed 35PN230 for their

Table 1. Design Specification of Analysis Models (Original Size).

Specification	Unit	Type A	Type B	Type C
Rotor Type	-	SPMSM	SPMSM	IPMSM
Magnetization Type	-	Parallel	Halbach	Parallel
Number of Poles	-	4	4	4
Number of Slots	-	24	24	24
Outer Dia. of Stator	mm	32.5	32.5	32.5
Inner Dia. of Stator	mm	17.3	17.3	17.3
Outer Dia. of Rotor	mm	16.5	16.5	16.5
Inner Dia. of Rotor	mm	7.5	7.5	7.5
Thickness of Sleeve	mm	2	2	-
Stack length	mm	48	48	48
Mechanical Air-gap	mm	0.4	0.4	0.4
PM Thickness	mm	3.5	3.5	2.3×9.3
PM Material	-	Sm2Co17	Sm2Co17	Sm2Co17
Number of Coil Turns	turns	56	56	56
Resistance	ohm	0.225	0.225	0.225
Induced voltage	V/1000rpm	3.7	3.7	3.7
Parallel Branch	-	2	2	2
Winding Connection	-	Y	Y	Y

stator and rotor core materials. This material is known that it can achieve higher efficiency than 50PN470 or 50PN1300 at low load torque with high speed as investigated in [8].

2.2. Equivalent Circuit Parameters

The representative equivalent circuit parameters of PM machines are induced voltage, resistance and inductance. Since the most machine characteristics are determined by those parameters, their accurate prediction is very essential.

At first, when it comes to the induced voltage, it can be obtained by (1) [9]. Here, A, S and θ are respectively magnetic vector potential, total areas of an N-turns and position of rotor. Since the integral of the magnetic vector potential is flux linkage, the induced voltage can be finally derived by differentiation of flux linkage value from finite element method (FEM).

$$e = -\frac{d}{d\theta}\left(\frac{\iint_s A\,ds}{S}\right) \tag{1}$$

In Fig. 2, the analyzed induced voltage of the analysis models in no-load condition is compared according to rotational speed. As shown in the figure, the machines show almost identical values in each speed condition, and the value at 1,000(rpm) is well corresponded to the measured value which will be presented later.

By contrast, in PM machines, the radius of the rotor shaft has high influence on machine performance, so the dimension should be carefully determined. Besides, in some applications, such as spindle motors or robots, its larger value is frequently required. Therefore, in this paper, the analysis also considers the radius of the rotor shaft. Figure 3 shows the analyzed induced voltage in no-load condition according to the rotor types and the radius of the rotor shaft. As can be confirmed in the figure, over 7.5(mm) of the radius, their values are being decreased. In particular, Type B, which is the SPMSM with Halbach magnetization, shows almost identical values until the radius is 9.0(mm). On the other hand, Type C, which is IPMSM with parallel magnetization, shows the most dramatic reduction. Therefore, it can be confirmed that the SPMSM type has benefits for large shaft applications, particularly Type B.

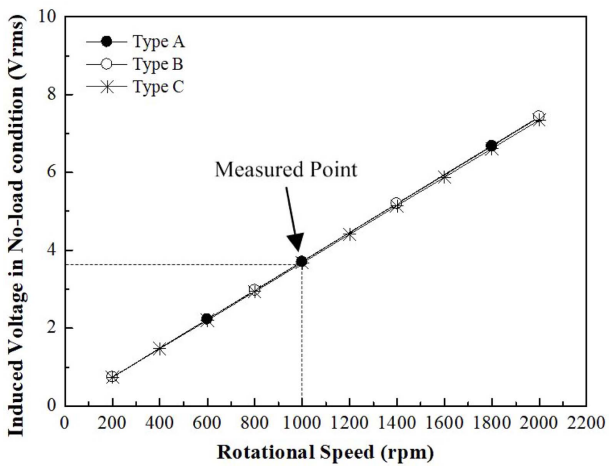

Fig. 2. Induced voltage of analysis models in no-load condition according to rotational speed.

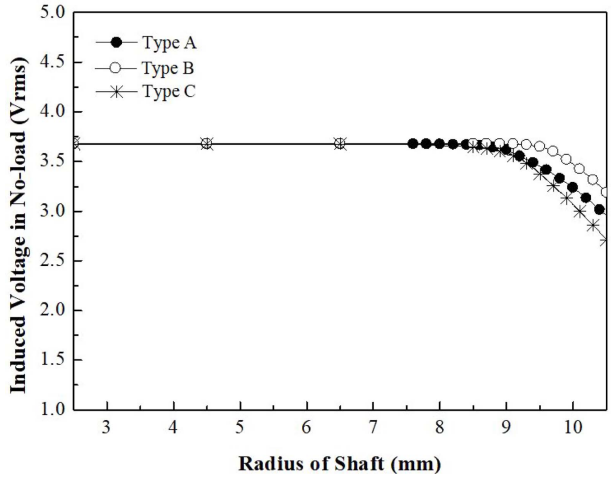

Fig. 3. Induced voltage in no-load condition according to radius of rotor shaft at 1,000(rpm).

In the second place, when it comes to resistance, since three analysis models employ the identical stator core, their resistance values are also identical. Using (2), the phase resistance can be achieved. Here, ρ, l, and A are resistivity at room temperature, total length of stator coil and cross sectional area of the coil. The predicted resistance value is presented in Table 1, and it will be compared with measured value later.

$$R_{ph} = \rho \cdot \frac{l}{A} \tag{2}$$

For the inductance calculation of PM machines, there were several studies, and this paper employed the vector control method [10]. The d-axis and q-axis inductance can be derived by (3)-(6). In those equations, d, q, V, I, ω_e, and Ψ are d-axis, q-axis, voltage, current, speed and flux linkage. In this study, the flux linkage values are obtained by electromagnetic field analysis based on FEM, and the resistance derived above is employed.

$$V_d = I_d R_{ph} - \omega_e \psi_q \tag{3}$$

$$V_q = I_q R_{ph} + \omega_e(\psi_d + \psi_{PM}) \tag{4}$$

$$L_d = (V_q / \omega_e - \psi_{PM}) / I_d \tag{5}$$

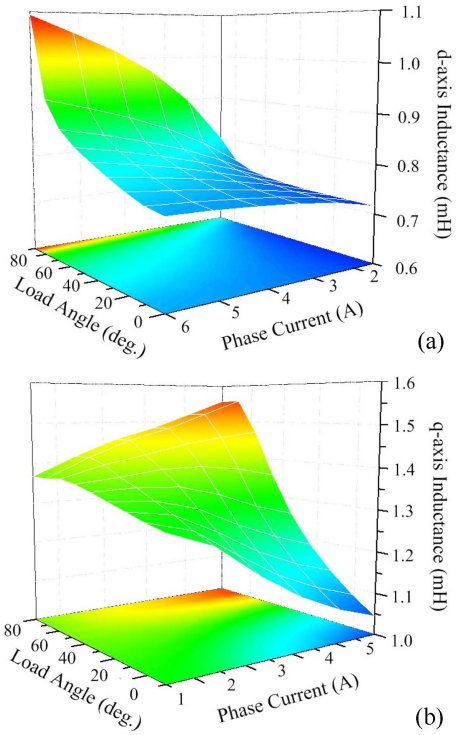

Fig. 4. (Color online) d-axis and q-axis inductance of IPMSM according to phase current and load angle: (a) d-axis inductance, (b) q-axis inductance.

$$L_q = V_d / (\omega_e I_q) \tag{6}$$

As it is very well known, the d-axis and q-axis inductance of the SPMSM are identical while the q-axis inductance is larger than the d-axis inductance when it comes to the IPMSM. Besides, it was reported that the inductance values are influenced by the saturation effect, current and load angle conditions [11], so the inductance variation by considering those variables are presented in Fig. 4. Those values are employed in the torque calculation below.

2.3. Torque

The torque of PMSMs can be expressed as (7), which are the summation of magnetic torque and reluctance torque [12]. Here, p is the number of pole pairs.

$$T = T_m + T_r = \frac{3}{2} p \left[\lambda_m I_q + (L_d - L_q) I_d I_q \right] \tag{7}$$

Since the SPMSM has identical d-axis and q-axis inductance, it has only magnetic torque while IPMSM has additional reluctance torque due to the difference of inductances. In this study, maximum torque per ampere (MTPA) is performed for each machine, and the torque curves are obtained according to rotational speed conditions as shown in Fig. 5. As shown in the figure, it is composed of constant torque region and constant power region.

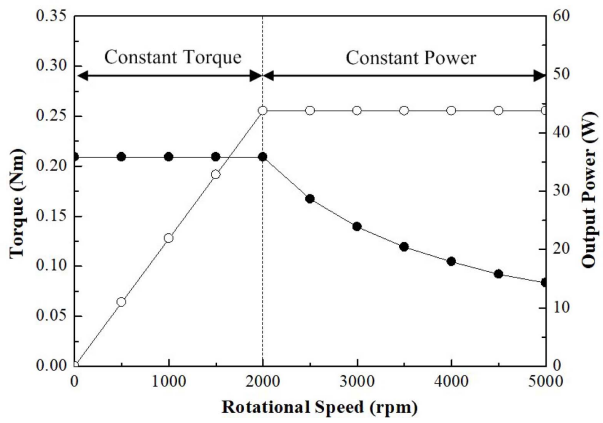

Fig. 5. Torque and output power characteristics of the analysis models according to rotational speed at rated current condition.

As it is very well known, the SPMSM does not have saliency, so the d-axis current is controlled to be zero while the flux weakening control is employed for constant power region as presented in [13]. On the other hand, for IPMSM, the load angle is determined to achieve maximum torque under base speed. Although SPMSM is generally known that it has poor flux weakening capability, it can be overcome by appropriate design of stator structure as the authors also showed in [13]. The analysis models in Table 1 are designed to have almost identical flux weakening capability to have the torque characteristic in Fig. 5.

As shown in the figure, its maximum speed is 5,000 (rpm) and the current density of stator coil winding is controlled under 5(A/mm^2). All the motors are controlled according to the torque and speed curves for their reasonable comparison.

2.4. Phase Current based on Dynamic Modeling of SVPWM Inverter System

The carrier frequency of the inverter has high influence on iron loss and PM eddy current loss as reported in [14]. In the previous study, the authors employed wave generator for input voltage, but the phase current of this paper is achieved from [15] which had performed the dynamic analysis with the modeling of SVPWM inverter and PMSMs based on derived machine parameters. Since the derived current contains the harmonics due to SVPWM inverter, they can be employed in power loss evaluation which is highly influence by them. In Fig. 6, the anticipated phase current is presented, and the electromag-

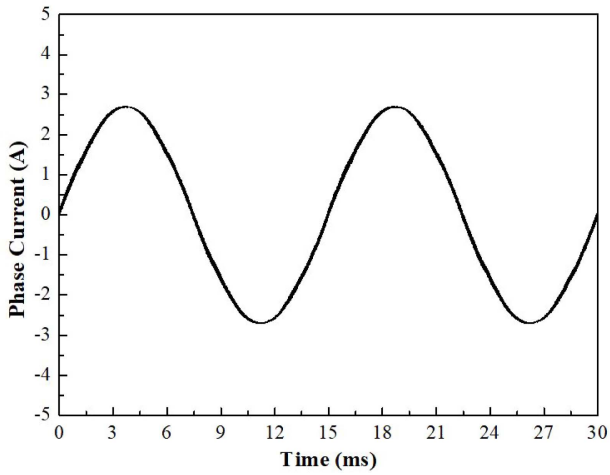

Fig. 6. Phase current waveform based on SVPWM inverter and dynamic modeling of PM machines at 2,000(rpm).

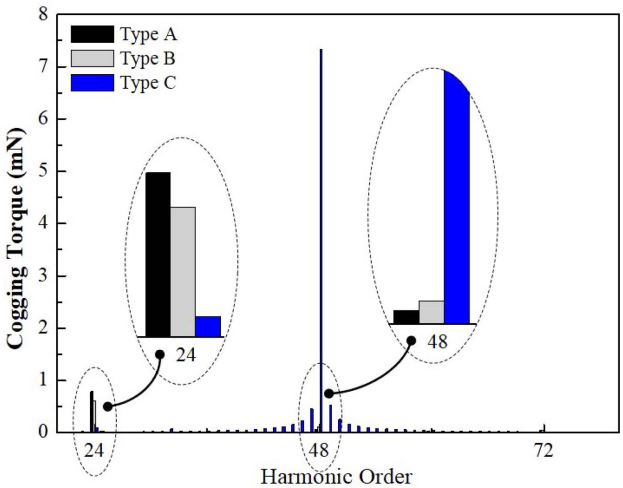

Fig. 7. (Color online) FFT result comparison of cogging torque in no-load condition.

netic field analysis is performed based on the current with harmonics.

2.5. Investigation on Vibration and Noise Sources

The electromagnetic sources of the vibration and noise in the motors are caused by three major reasons, and they are cogging torque, torque ripple and radial force stress as shown in [16]. The authors in the previous study showed that the FFT results of the vibration and noise are well corresponded to those of the electromagnetic sources. For 4 pole and 24 slot combination, the 24*nf*, 6*nf* and 4*nf* harmonic orders are generated by cogging torque, torque ripple and radial force density with the influence of phase current. Here, *n* and *f* are respectively harmonic order and frequency.

The cogging torque can be calculated by integrating the multiplied value of the radial component of flux density by the tangential component of flux density as shown in (8) [16]. It can be also known that the length of rotor and axial length have high influence on the cogging torque. Here, B_r and B_t are respectively the radial component and the tangential component of the flux density while L, R and μ_0 are respectively axial length, radial length and permeability of vacuum.

$$T_c = \frac{LR^2}{\mu_0}\int B_r B_t d\theta \tag{8}$$

In Fig. 7, the FFT results of cogging torque according to machine types are presented. Here, inner diameter of rotor core is 7.5(mm). As previously reported, 24*nf* order shows visible values. While Type A shows highest value in 24th order, Type C shows much higher values in 48th order. By summation of all the harmonic orders, Type C has high cogging torque characteristic.

On the other hand, the torque ripple is generated by the harmonic combination of induced voltage and phase current, for example, 1st component of induced voltage and 5th component of phase current, 3rd component of induced voltage and 3rd component of phase current and 5th component of induced voltage and 1st component of phase current.

In Fig. 8, the FFT results of the torque ripple according to the analysis models are presented at rated speed condition. Here, the phase current and load angle are applied to achieve the torque-speed curve presented in Fig. 5. As can be confirmed in the figure, while the fundamental order shows almost identical values, Type C shows highest value in every 6*nf* orders. When it comes to SPMSM types, Type A shows higher torque ripple than

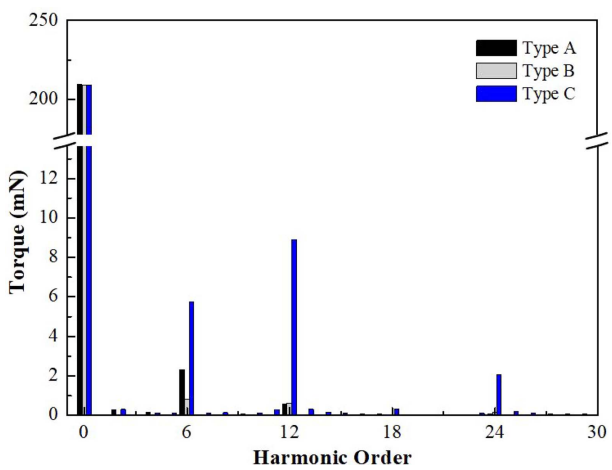

Fig. 8. (Color online) FFT result comparison of torque ripple in rated load condition.

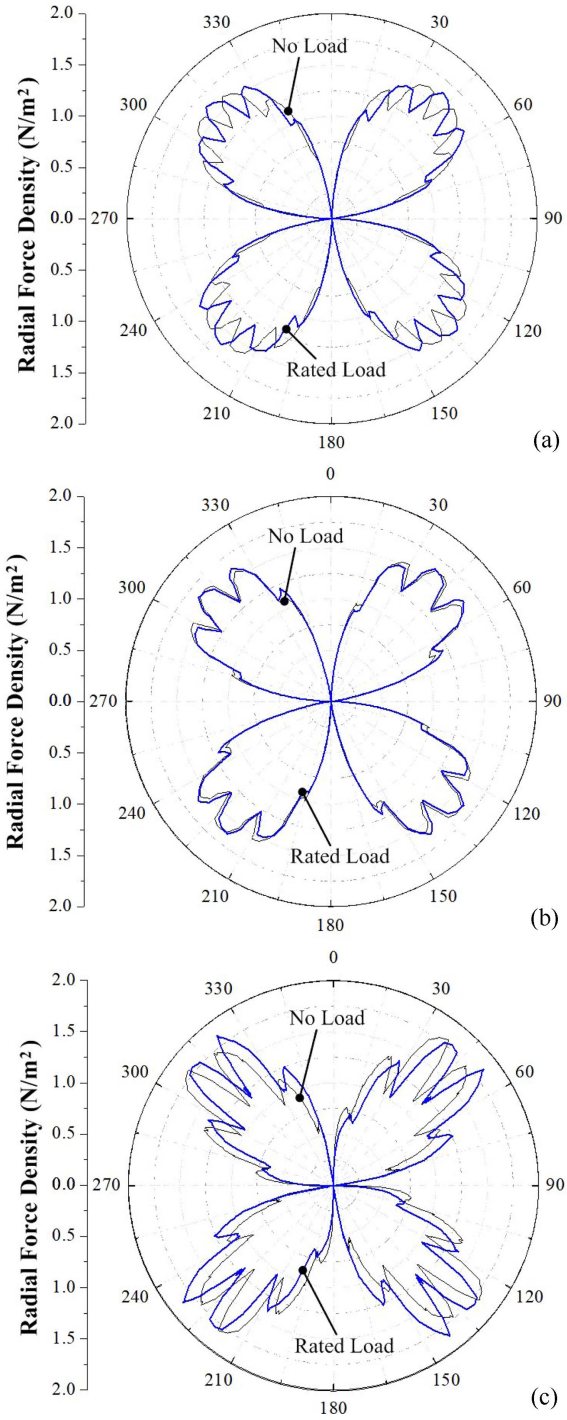

Fig. 9. (Color online) Radial force density of no-load and rated load condition (2A with SVPWM inverter: (a) Type A, (b) Type B, (C) Type C.

Type B, particularly in 6th order.

Lastly, the radial force density can be achieved by the radial component and the tangential component of flux density based on electromagnetic field analysis as shown in (9) [17].

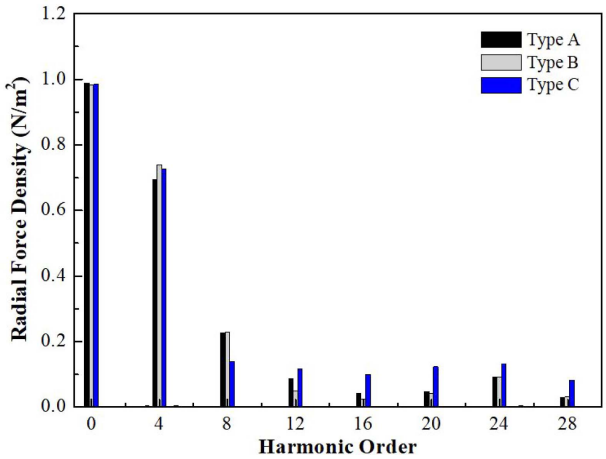

Fig. 10. (Color online) FFT result comparison of radial force density in rated load condition.

$$F_r = \frac{\left(B_r^2 - B_t^2\right)}{2\mu_0} \tag{9}$$

Figure 9 compares the radial force density derived from those equations and each component of flux density. The values are obtained according to load conditions which are no-load and 2(A) of phase current with SVPWM inverter. As can be confirmed in the figure, Type C is most highly influenced by the phase current while Type B, which is the SPMSM with Halbach magnetization, has very little visible difference. Besides, it can be also known that the SPMSM types show little less value of radial force density in comparison with IPMSM type.

Figure 10 shows FFT results of the radial force density. As mentioned above, *4nf* harmonic orders are dominant. In the figure, while the fundamental harmonic is almost identical, and Type C shows less value than the other types when n=1 and 2 which is low order level. On the other hand, Type C shows much higher values when n=3, 4, 5, 6 and 7.

3. Experimental Verification with Manufactured Machines and Performance Evaluation

3.1. Manufactured Machine and Test Results

In this study, for the experimental verification, manufactured Type C is employed as shown in Fig. 11. The material of housing is nickel-coated SM45C, the manufactured machine is directly connected to an operating motor for mechanical input power. Figure 12 presents the measured phase voltage of manufactured Type C (IPMSM) in no-load condition. In this experiment, the rotational speed of the induction motor directly connected to the

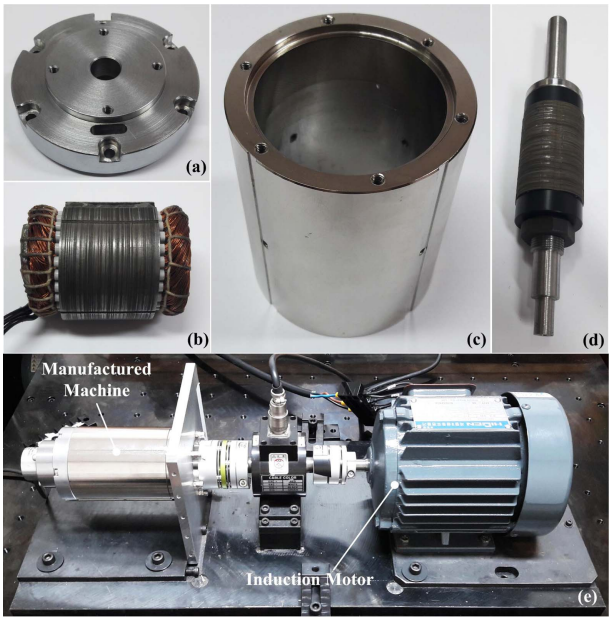

Fig. 11. (Color online) Manufactured machine and experimental set construction : (a) housing cover, (b) stator, (c) housing, (d) rotor, (e) assembly with operating motor.

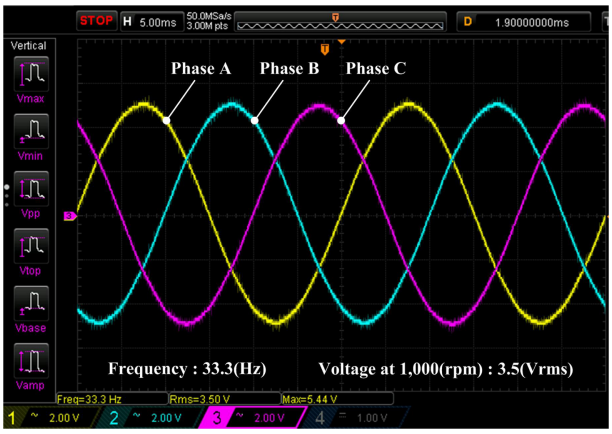

Fig. 12. (Color online) Measured phase voltage of Type C (IPMSM Type) at 1,000(rpm) in no-load condition.

manufactured machine was 1,000(rpm), and the three load resistors with high-value 1(kohm) are y-connected to each phase. The waveforms are the voltage in the load resistors. Here, the measured value of the stator coil resistance is 0.23(ohm). Since the value of those load resistors is much higher than that of the stator coil resistance, the waveforms can be regarded as the phase voltage in no-load condition. In comparison with the analysis results in Fig. 2, it can be confirmed that the values are very similar.

On the other hand, Fig. 13 shows the measured phase current while it is controlled to be 2(A) at 2,000(rpm).

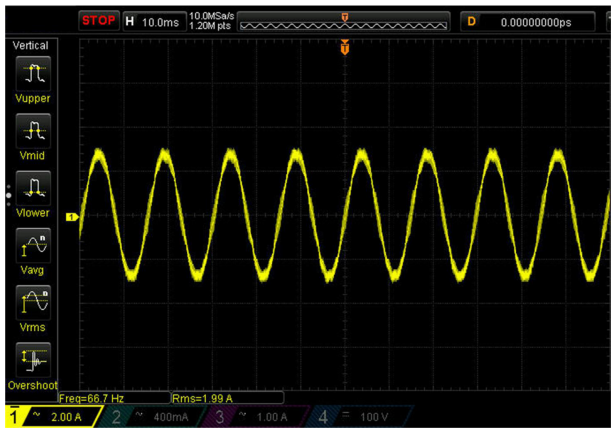

Fig. 13. (Color online) Measured phase current of Type C (IPMSM) at 2,000(rpm).

The phase current was predicted in Fig. 6.

3.2. Power Loss and Efficiency Evaluation

The power losses dealt with in this paper are copper loss, core loss and rotor loss which are all the electrical losses while the mechanical losses, such as friction and windage loss, are not addressed. On the other hand, to investigate the influence of the shaft size on the machine performance, the radius of shaft condition 7.5(mm) and 10.5(mm) are selected for comparative analysis.

At first, the copper loss P_c is estimated by multiplying the square of phase current and resistance, which was derived above. When the rotational speed is increased, the phase resistance is also increased due to skin effect. As can be confirmed in equation (10) to calculate the penetration [18], the area for current flow is determined by the frequency, the permeability, the conductivity of employed copper coil winding. Here, f, μ_r, μ_0 and σ are frequency, permeability in vacuum and relative permeability and conductivity. By considering the skin depth more accurate resistance can be estimated.

$$d = \frac{1}{\sqrt{\pi f \mu_r \mu_0 \sigma}} \tag{10}$$

In addition, as shown in Fig. 3, since the induced voltage is reduced when the value is over 7.5(mm), the

Table 2. Phase Current for Required Torque Characteristic and Copper Loss according to Machine Types and Radius of Shaft.

Model	7.5(mm)		10.5(mm)	
	Current (A)	P_c (W)	Current (A)	P_c (W)
Type A	2.0	1.02	2.4	1.55
Type B	2.0	1.02	2.2	1.32
Type C	2.0	1.02	2.6	1.84

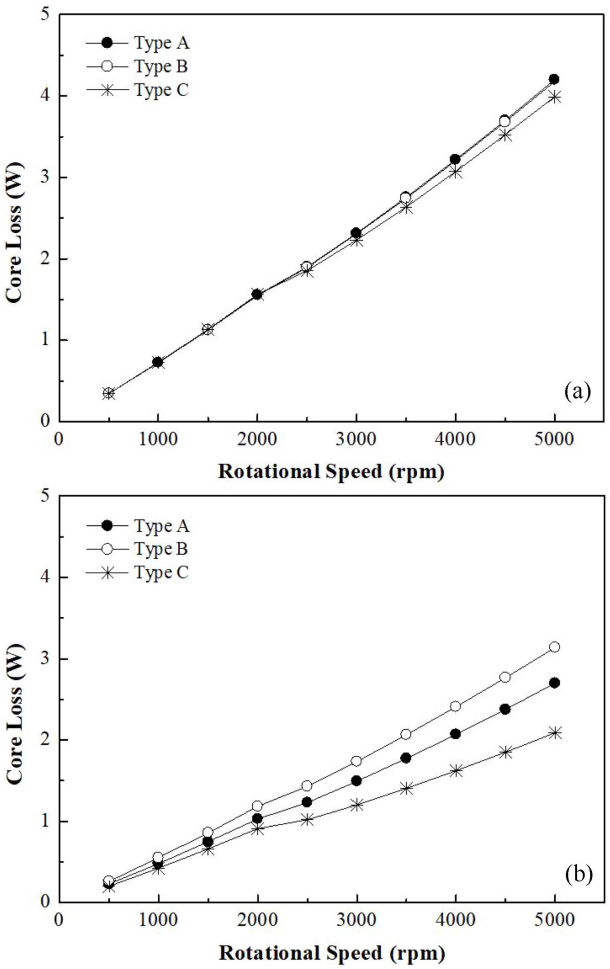

Fig. 14. Analyzed core loss comparison according to rotational speed: (a) shaft radius = 7.5(mm), (b) shaft radius = 10.5(mm).

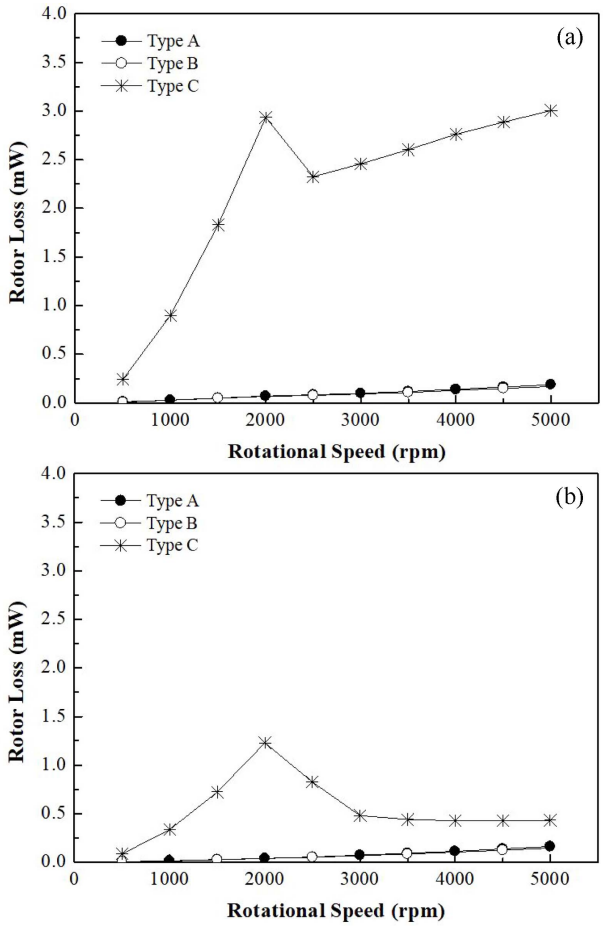

Fig. 15. Analyzed rotor loss comparison according to rotational speed: (a) shaft radius = 7.5(mm), (b) shaft radius = 10.5(mm).

higher current value is required for the torque characteristic presented in Fig. 5, and more detailed values are presented in Table 2.

In the second place, the core loss can be achieved by (11) [19], and it is composed of hysteresis loss and eddy current loss. Since the simulation is performed based on the current of the SVPWM inverter, its harmonics are also considered as well. In the equation k_h, and k_e are respectively the constant of hysteresis and eddy current while l is the harmonic order

$$P_i = \sum_{l=1}^{\infty}(k_{hl} f_l B_l^n + k_{el} f_l^2 B_l^2) \tag{11}$$

In Fig. 14, the core loss characteristics are compared according to machine types and the radius of the rotor shaft. When the radius of the rotor shaft is 7.5(mm), the core loss is very similar since the flux density in the core is almost identical. This is also easily anticipated from the induced voltage mentioned above. On the other hand, when the radius of shaft is 10.5(mm), visible difference can be found. In other words, Type B shows the highest value while Type C shows the lowest value. This is also resulted from the difference of the flux density in the core, and the same order can be found in the induced voltage characteristics.

Lastly, in Fig. 15, the rotor loss characteristics are compared in identical condition as dealt with above. As can be confirmed in the figures, Type A and B show almost identical values in spite of the difference of radius of the rotor shaft. On the other hand, when it comes to Type C, the rotor loss is reduced when the radius of the rotor shaft is 10.5(mm). However, the value is still very low, so the rotor losses of those machines have very low influence on the motor performance.

The efficiency can be obtained by previously achieved motor parameters and losses based on (12). Here, P_{in}, P_{out}, P_c, P_i, and P_r are respectively input power, output power, copper loss, core loss and rotor loss.

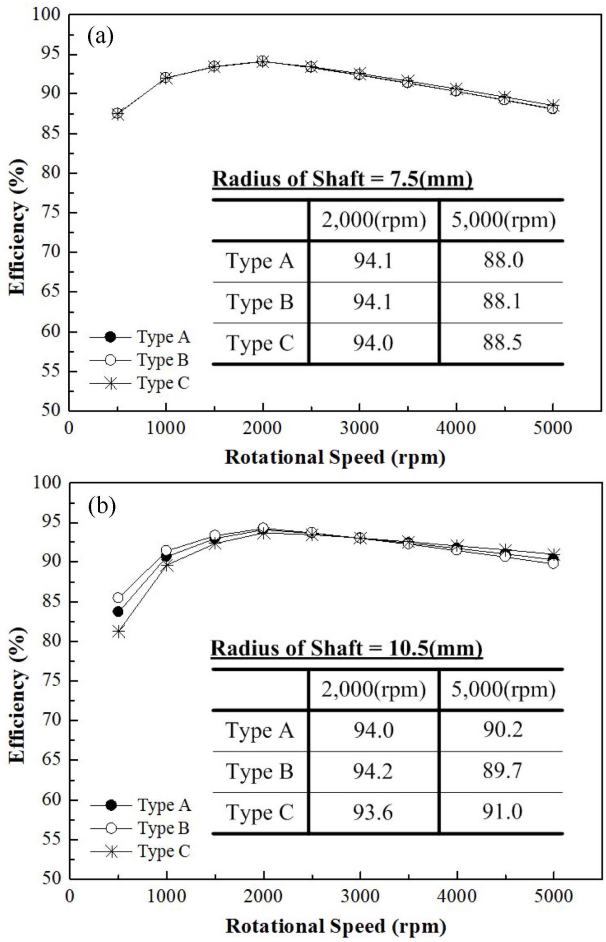

Fig. 16. Efficiency comparison according to rotational speed: (a) shaft radius = 7.5(mm), (b) shaft radius = 10.5(mm).

$$\eta = \frac{P_{out}}{P_{in}} = \frac{\omega T}{P_{out} + P_c + P_i + P_r} \tag{12}$$

In Fig. 16, the efficiency is compared according to the machine types and the radius of the rotor shaft. As it can be estimated from the power loss characteristics, the values are very similar when the radius of shaft is 7.5(mm). On the other hand, when it is 10.5(mm), a bit little difference can be found. In particular, in low speed condition, the difference is large with the highest value of Type B. In high speed condition, Type C shows the highest value.

On the other hand, according to the materials of the stator core, the efficiency can be improved. In [20], the authors also calculated the copper loss and core loss with similar method. In the previous study, by using the amorphous core (0.025t), 98.46(%) of efficiency was achieved for SPMSM in turbocharger system. However, the material is not costly effective, and 35PN440 from POSCO shows approximately 95(%) which is similar level of the analysis models in this paper.

4. Conclusion

In this paper, three types of PMSMs were comparatively investigated. Those machines have different rotor structure according to magnetization patterns while the machine size was identical. Based on electromagnetic field analysis, their equivalent circuit parameters were derived, and their performance was also evaluated by including torque characteristics, radial force and power losses. Besides, one of the analysis models was manufactured for experimental verification. Based on the evaluation results, following conclusion can be made. At first, when the rotor shaft is 7.5(mm), their efficiency shows similar performance, but, in high speed condition, Type C shows less core loss. Therefore, other types require more efforts to reduce the loss for performance improvement. On the other hand, when the rotor shaft is 10.5(mm), Type C presented highest efficiency in high speed region. Although this study addressed small scale machines, the derived results can be referred to the design of larger scale applications.

Acknowledgment

This was supported by Korea National University of Transportation in 2020.

References

[1] D. K. Hong, J. H. Choi, D. J. Kim, Y. D. Chun, B. C. Woo, and D. H. Koo, IEEE Trans. Magn. **49**, 7 (2013).
[2] C. C Hwang, S. S. Hung, C. T. Liu, and S. P. Cheng, IEEE Trans. Magn. **50**, 1 (2014).
[3] Z. Q. Zhu, Z. P. Xia, Y. F. Shi, D. Howe, A. Pride, and X. J. Chen, IEEE Trans. Magn. **39**, 5 (2003).
[4] K. Liu, M. Yin, W. Hua, Z. Ma, M. Lin, and Y. Kong, IEEE Trans. Magn. **54**, 11 (2018).
[5] M. Markovic and Y. Perriard, IEEE Trans. Magn. **45**, 7 (2009).
[6] Duane Hanselman, E-Man Press LLC (2012).
[7] Fang Deng and Thomas W. Nehl, IEEE Trans. Magn. **34**, 5 (1998).
[8] S. O. Kwon, J. J. Lee, B. H. Lee, J. H. Kim, K. H. Ha, and J. P. Hong, IEEE Trans. Magn. **45**, 10 (2009).
[9] K. T. Kim, K. S. Kim, S. M. Hwang, T. J. Kim, and Y. H. Jung, IEEE Trans. Magn. **37**, 5 (2001).
[10] R. Dutta and M. F. Rahman, IEEE Trans. Magn. **42**, 11 (2006).
[11] K. J. Meessen, P. Thelin, J. Soulard, and E. A. Lomonova, IEEE Trans. Magn. **44**, 10 (2008).

[12] T. A. Huynh and M. F Hsieh, IEEE Trans. Magn. **53**, 11 (2017).
[13] Z. Q. Zhu, Z. P. Xia, Y. F. Shi, D. Howe, A. Pride, and X. J. Chen, IEEE Trans. Magn. **39**, 5 (2003).
[14] K. Yamazaki and Y. Togashi, IEEE Trans. Magn. **54**, 3 (2018).
[15] Y. S. Park, M. M. Koo, S. M. Jang, J. Y. Choi, and D. J. You, IEEE Trans. Magn. **5**, 11 (2014).
[16] H. S. Ko and K. J. Kim, IEEE Trans. Magn. **40**, 6 (2004).
[17] S. Yu and R. Tang, IEEE Trans. Magn. **42**, 4 (2006).
[18] O. Payza, Y. Demir, and M. Aydin, IEEE Trans. Magn. **54**, 11 (2018).
[19] D. K. Hong J. Y. Lee, B. C. Woo, D. H. Park, and B. U. Nam, IEEE Trans. Magn. **48**, 11 (2012).
[20] D. K. Hong, T. W. Lee, and Y. H. Jeong, IEEE Trans. Magn. **54**, 11 (2018).